GEOPHYSICS, VOL. 84, NO. 2 (MARCH-APRIL 2019); P. KS13–KS27, 11 FIGS.
10.1190/GEO2018-0251.1

Check for updates

Downloaded 03/14/19 to 138.67.129.23. Redistribution subject to SEG license or copyright; see Terms of Use at http://library.seg.org/

3D passive wavefield imaging using the energy norm

Daniel Rocha[1], Paul Sava[1], Jeffrey Shragge[2], and Ben Witten[3]

ABSTRACT

In passive seismic monitoring of microseismicity, full-wavefield imaging offers a robust approach for the estimation of source location and mechanism. With multicomponent data and the full 3D anisotropic elastic wave equation, the coexistence of P- and S-modes at the source location in time-reversal wavefield extrapolation allows the development of imaging conditions that identify the source position and radiation pattern. We have developed an imaging condition for passive wavefield imaging that is based on energy conservation and is related to the source mechanism. Similar to the correlation between the decomposed P- and S-wavefields — the most common imaging condition used in passive elastic wavefield imaging — our proposed imaging condition compares the different modes present in the displacement field producing a strong and focused correlation at the source location without costly wave-mode decomposition at each time step. Numerical experiments demonstrate the advantages of the proposed imaging condition (compared to PS correlation with decomposed wave modes), its sensitivity with respect to velocity inaccuracy, and its quality and efficacy in estimating the source location.

INTRODUCTION

Passive seismic monitoring uses signals caused by either natural or induced seismicity to infer earthquake locations, source mechanisms, and subsurface properties. Its differences with respect to conventional exploration seismology mainly consist of the absence of a controlled source, but also of distinct array geometries, continuous recording times, and low signal-to-noise ratios (S/Ns), among others. Although the source locations for passive seismic scenario are unknown a priori, one can apply imaging and inversion methods adapted from active source seismic scenarios to generate an image, showing the estimated source location, and/or to reconstruct a 3D earth model, with information about subsurface physical properties (Duncan and Eisner, 2010; Maxwell et al., 2010; Xuan and Sava, 2010; Behura et al., 2013; Blias and Grechka, 2013; Douma and Snieder, 2015; Witten and Shragge, 2015; Bazargani and Snieder, 2016; Witten and Shragge, 2017a, 2017b).

In oil and gas exploration, passive seismic monitoring is commonly termed microseismic monitoring (Warpinski et al., 2012; Maxwell, 2014; Grechka and Heigl, 2017) because this type of induced seismicity typically has low orders of moment magnitudes (i.e., $M_w \leq 0$). Microseismic monitoring is a powerful technique for obtaining production attributes from unconventional reservoirs, especially when investigating hydraulic fracturing. Where fluid injection into a reservoir induces microseismicity observable from surface or borehole monitoring arrays, one can use recorded data to estimate microseismic source locations and thereby gain insight as to where hydraulic fracturing is occurring in the subsurface (Maxwell, 2010; Michel and Tsvankin, 2013). Beyond source location estimation, microseismic monitoring (using a catalog of detected events) facilitates other useful applications such as estimating source mechanisms, which potentially provides geomechanical information such as fault and fracture orientation (Jeremic et al., 2014; Zhebel and Eisner, 2015).

One common approach for analyzing microseismic data involves applying a Kirchhoff-based migration algorithm to stack windowed events along traveltime trajectories and over all possible source initiation times, assuming a sufficiently accurate velocity model (Kao and Shan, 2004; Baker et al., 2005). However, such an approach does not stack over the full waveform and implicitly relies on strong assumptions about velocity model accuracy and associated wave propagation effects (e.g., neglecting multipathing) that are not appropriate for realistic scenarios. Alternatively, approaches based on wave-equation migration have gained interest for passive seismic imaging (Artman et al., 2010; Xuan and Sava, 2010; Witten and

Manuscript received by the Editor 5 April 2018; revised manuscript received 22 August 2018; published online 26 February 2019.
[1]Colorado School of Mines, Center for Wave Phenomena, Golden, Colorado, USA. E-mail: drocha@mines.edu (corresponding author); psava@mines.edu.
[2]Formerly University of Western Australia, Crawley, Australia; presently Colorado School of Mines, Center for Wave Phenomena, Golden, Colorado, USA. E-mail: jeffrey.shragge@uwa.edu.au.
[3]University of Western Australia, School of Earth Sciences, Norman, Australia. E-mail: bwitten@gmail.com.
© 2019 Society of Exploration Geophysicists. All rights reserved.

Downloaded 03/14/19 to 138.67.129.23. Redistribution subject to SEG license or copyright; see Terms of Use at http://library.seg.org/

Shragge, 2015; Nakata and Beroza, 2016) because they use the full waveform of these signals (beyond stacking along traveltime trajectories), accurately handle wave propagation in complex earth models, and offer a range of imaging conditions that effectively stack over the full microseismic waveform.

Full-wavefield imaging adapted to the problem of estimating microseismic source locations is usually implemented in two steps: (1) time-reversed wavefield extrapolation (or backpropagation) of the recorded wavefield into an earth model and (2) application of an imaging condition to extract the source location and/or origin time from the extrapolated wavefield (McMechan, 1982; Gajewski and Tessmer, 2005; Xuan and Sava, 2010; Nakata and Beroza, 2016). Generally, the imaging condition involves computing the zero-lag autocorrelation of the 4D wavefield, collapsing it into a 3D image volume. Assuming a correct velocity model and proper treatment of source-radiation patterns, the peak amplitude of the image corresponds to the true source location; however, not satisfying these assumptions can often lead to severe mislocation of imaged events. To address velocity model inaccuracy, it is insufficient to rely solely on zero-lag wavefield autocorrelation to provide information for velocity improvement. As explored in active seismic scenarios (Rickett and Sava, 2002; Sava and Fomel, 2006; Sava and Vasconcelos, 2011; Yang and Sava, 2015) and more recently in passive seismic ones (Witten and Shragge, 2015), wavefield correlation beyond zero lag generates so-called extended images (because they represent an extension of zero-lag images), which provide the sufficient and necessary information to improve the migration velocities within the adjoint-state tomography framework (Witten and Shragge, 2017a).

For multicomponent microseismic data, one typically uses wave extrapolation and imaging procedures that exploit distinct elastic wave modes. The colocation of P- and S-wavefields at the source-excitation point allows for a PS imaging condition (PSIC) to be implemented in three steps: (1) elastic (or pseudoelastic) backpropagation of the recorded multicomponent wavefield, (2) wave-mode decomposition of the back-propagated displacement field, and (3) crosscorrelation of the two P- and S-wavefields (Artman et al., 2010; Witten and Artman, 2010). However, especially in 3D applications involving an anisotropic medium, step (2) is computationally expensive; thus it impedes a quick and robust imaging implementation because it must be repeated at each extrapolation time step. Another shortcoming of the elastic PS correlation is that it does not properly handle the different polarization directions at the locus of maximum P- and S-phase correlation, producing a nodal plane (i.e., a zero) at the actual source location. Ideally (and especially in the presence of a low S/N), one would expect to encounter the peak amplitude at the source position; to expect otherwise would pose interpretation and inversion challenges.

We aim to address these shortcomings of the multicomponent elastic PSIC that are detrimental to the source-location identification and migration velocity analysis of microseismic data. By substituting PS for energy correlation (Rocha et al., 2016b, 2017), we propose an energy passive imaging condition (EPIC) that has five key advantages over conventional PSIC: (1) It naturally accounts for source-radiation patterns, (2) it produces a peak image amplitude at the estimated source location, (3) it precludes the need for wave-mode decomposition at each time step, (4) it downweights the correlation between common wave modes (i.e., PP and SS) away from the source, while enhancing the correlation of different wave modes (i.e., PS) at the source location, and (5) it offers a straightforward complement to extended image attributes that are important for microseismic migration velocity analysis based on the temporal separation of P- and S-wave arrivals. For the purpose of improving image quality, we implement a wave-mode separation — advantage (3) — only once in the data domain.

In this paper, we review the theory of elastic modeling and associated conventional imaging conditions; we introduce the energy imaging condition, originally developed for active-source wavefield imaging — elastic reverse time migration (ERTM); and we detail how we adapt it to passive seismic scenarios. Then, we present the extended-domain versions of PSIC and energy imaging condition and we show a novel methodology applied in our numerical experiments to mitigate imaging artifacts, albeit with an increase in computational cost. We demonstrate our methodology with 3D synthetic examples of increasing complexity, as well as with field data. The paper concludes with a discussion of the merits and caveats of our method, and with suggestions for further refinement of the method.

THEORY

In this section, we review the elastic wave equations used in full-wavefield imaging, as well as the most commonly used imaging conditions for multicomponent passive data. Then, we propose an imaging condition based on the energy norm for elastic wavefields. Finally, we introduce the extended version of our proposed imaging condition that is potentially important for velocity-estimation applications.

Elastic modeling

The elastic wave equation in the absence of external sources may be written as (Aki and Richards, 2002)

$$\rho\ddot{\mathbf{U}} = \nabla \cdot \left[\underline{\underline{\mathbf{c}}}\nabla\mathbf{U}\right], \tag{1}$$

where $\mathbf{U}(\mathbf{x}, t)$ is the displacement field as a function of space ($\mathbf{x}$) and time (t), $\rho(\mathbf{x})$ is the medium density, and $\underline{\underline{\mathbf{c}}}(\mathbf{x})$ is the fourth-rank stiffness tensor. A superscript dot on the displacement field indicates first-order time differentiation. If we assume a slowly varying isotropic medium, equation 1 reduces to

$$\rho\ddot{\mathbf{U}} = (\lambda + 2\mu)\nabla(\nabla \cdot \mathbf{U}) - \mu\nabla \times (\nabla \times \mathbf{U}), \tag{2}$$

where $\lambda(\mathbf{x})$ and $\mu(\mathbf{x})$ are the Lamé parameters. Equation 2 can be written as a function of velocities by substituting $V_{\mathrm{P}}^2 = (\lambda + 2\mu)/\rho$ and $V_{\mathrm{S}}^2 = \mu/\rho$:

$$\ddot{\mathbf{U}} = V_{\mathrm{P}}^2\nabla(\nabla \cdot \mathbf{U}) - V_{\mathrm{S}}^2\nabla \times (\nabla \times \mathbf{U}), \tag{3}$$

where $V_{\mathrm{P}}(\mathbf{x})$ and $V_{\mathrm{S}}(\mathbf{x})$ are the P- and S-wave velocities, respectively. Using multicomponent data recorded at the receivers, a displacement field $\mathbf{U}$ can be extrapolated forward or backward in time throughout a subsurface model using either equation 1 or 3, depending on the assumptions about anisotropy of the medium. Although more realistic in nature, incorporating anisotropy involves complex phenomena such as S-wave splitting (Crampin, 1985; Alford, 1986), which introduces two S-wave modes with different polarizations and phase velocities in wavefield extrapolation. Without loss of generality, we assume isotropy in the following numerical experiments so as

Downloaded 03/14/19 to 138.67.129.23. Redistribution subject to SEG license or copyright; see Terms of Use at http://library.seg.org/

to analyze only a single S-wave mode (and for clarity purposes). We discuss the extension of our imaging approach to anisotropic media in the "Discussion" section.

Passive imaging conditions: Autocorrelation

Different imaging conditions acting directly on the wavefield displacement have been proposed for estimating the source locations in passive wavefield imaging (Steiner et al., 2008; Jeremic et al., 2015). For instance, Steiner et al. (2008) propose to use the absolute value of the particle velocity, i.e., the time derivative of the displacement vector field, whereas Saenger (2011) presents an imaging condition based on the product between the stress and strain fields. More commonly, one implements wave-mode decomposition of the extrapolated displacement field into its P- and S-wavefield constituents, typically implemented using Helmholtz decomposition operators (Dellinger and Etgen, 1990; Yan and Sava, 2009):

$$P = \nabla \cdot \mathbf{U}, \tag{4}$$

$$\mathbf{S} = \nabla \times \mathbf{U}, \tag{5}$$

where $P(\mathbf{x}, t)$ is a scalar wavefield containing the P-wave mode and $\mathbf{S}(\mathbf{x}, t)$ is a vector wavefield containing the transverse wave mode.

Because a scalar wavefield image is generally preferable to a vector or tensor image, but the S-wavefield from this decomposition remains a 3D vector field, passive imaging conditions can use the energy densities E_P and E_S of the decomposed P- and S-wavefields (Morse and Feshbach, 1953):

$$E_P(\mathbf{x}, t) = \|P\|, \tag{6}$$

$$E_S(\mathbf{x}, t) = \|\mathbf{S}\|, \tag{7}$$

where $\|\cdot\|$ indicates the magnitude of a scalar or vector wavefield. Separated wave modes and their energy densities allow one to implement autocorrelation passive imaging conditions:

$$I_{\mathrm{PP}}(\mathbf{x}) = \sum_t P(\mathbf{x}, t) P(\mathbf{x}, t) \equiv \sum_t E_P^2(\mathbf{x}, t), \tag{8}$$

$$I_{\mathrm{SS}}(\mathbf{x}) = \sum_t \mathbf{S}(\mathbf{x}, t) \cdot \mathbf{S}(\mathbf{x}, t) \equiv \sum_t E_S^2(\mathbf{x}, t). \tag{9}$$

Passive imaging conditions: Crosscorrelation

A recurrent problem with the imaging conditions in equations 8 and 9 is that the correlation of the wavefield with itself produces low-wavenumber content along the propagation path, e.g., between the source in the subsurface and the receivers on the surface or in a borehole. The same problem occurs with imaging conditions that directly use the displacement field in the absence of wave-mode decomposition. This poses significant challenges for microseismic migration and inversion-based analyses that require tightly focused event images.

Alternatively, one can use the different modes of the displacement field to define an imaging condition free of low-wavenumber autocorrelation artifacts. For a nonscattering medium and assuming an impulsive source event, extrapolated P- and S-waves from a single microseismic event propagate at different speeds and only coexist in space and time at the vicinity of the source location and at the initiation time. Exploiting this fact, one can define a PSIC (Artman et al., 2010):

$$\mathbf{I}_{\mathrm{PS}}(\mathbf{x}) = \sum_t P(\mathbf{x}, t) \mathbf{S}(\mathbf{x}, t), \tag{10}$$

where $\mathbf{I}_{\mathrm{PS}}(\mathbf{x})$ is a vector image, whose individual components represent the correlation between $P(\mathbf{x}, t)$ and the corresponding components of $\mathbf{S}(\mathbf{x}, t)$. Yan and Sava (2008) also propose a similar PSIC, but in the context of ERTM. However, one drawback is that, in a 3D experiment, three images are available instead of a scalar one concisely showing the source location. Considering this, one could conveniently compute a scalar PS image using the S-wave energy density in equation 7:

$$I_{\mathrm{PS}}(\mathbf{x}) = \sum_t P(\mathbf{x}, t) E_S(\mathbf{x}, t). \tag{11}$$

For isotropic media, equation 11 is quite straightforward to implement; however, this is not the case in anisotropic media for which wave-mode decomposition is significantly more expensive to compute (Dellinger and Etgen, 1990; Zhang and McMechan, 2010; Yan and Sava, 2011; Cheng and Fomel, 2014). Also, the PS correlation — either in equation 10 or 11 — produces a zero amplitude at the source location and an associated nodal plane, whose positive and negative side lobes suggest the source localization at the zero crossing. Although preprocessing techniques exist to address this problem (Eisner et al., 2008; Ay et al., 2012; Witten and Shragge, 2015), they lead to lower frequency wavefields and loss of spatial resolution.

Energy norm imaging conditions

In contrast, the energy norm (Rocha et al., 2016a, 2016b) allows one to define a pair of imaging conditions for many applications, with no difficulty in its implementation regardless of the anisotropy of the medium. In that context, this pair of imaging conditions is defined as (Rocha et al., 2017)

$$I_E^H(\mathbf{x}) = \sum_t [\rho \dot{\mathbf{U}} \cdot \dot{\mathbf{V}} + (\underline{\underline{\mathbf{c}}} \nabla \mathbf{U}) : \nabla \mathbf{V}], \tag{12}$$

$$I_E^L(\mathbf{x}) = \sum_t [\rho \dot{\mathbf{U}} \cdot \dot{\mathbf{V}} - (\underline{\underline{\mathbf{c}}} \nabla \mathbf{U}) : \nabla \mathbf{V}], \tag{13}$$

where $\mathbf{U}(\mathbf{x}, t)$ and $\mathbf{V}(\mathbf{x}, t)$ are two state wavefields and the symbol : indicates the Frobenius product (Golub and Loan, 1996). The imaging condition in equation 12 represents the temporal integration of the total energy product between the two wavefields, whereas that in equation 13 is a differential energy measure that attenuates events within the two wavefields sharing the same polarization and propagation direction. The correlation between such events generates the aforementioned detrimental low-wavenumber artifacts. Rocha et al. (2017) successfully use the imaging condition in

Downloaded 03/14/19 to 138.67.129.23. Redistribution subject to SEG license or copyright; see Terms of Use at http://library.seg.org/

equation 13 for ERTM (where $\mathbf{U}(\mathbf{x}, t)$ and $\mathbf{V}(\mathbf{x}, t)$ are the source and receiver wavefields), suppressing these artifacts and concisely imaging subsurface reflectors.

For passive imaging, where we extrapolate a single wavefield containing all wave modes, we can also define a pair of autocorrelation imaging conditions by establishing $\mathbf{U} = \mathbf{V}$ in equations 12 and 13. With such substitution, the individual terms have a special meaning in reference to the energy of the elastic wavefield: The first and second terms in equations 12 and 13 represent the kinetic and potential energies of the single wavefield, respectively. Therefore, equation 12 is related to the Hamiltonian operator (the superscript H stands for Hamiltonian), which measures the total wavefield energy, whereas equation 13 is related to the Lagrangian operator (superscript L stands for Lagrangian), defined as the difference between kinetic and potential energy terms (Ben-Menahem and Singh, 1981). We note that Saenger (2011) uses the potential term alone as an imaging condition, but here we extend this approach by combining kinetic and potentials terms to effectively mitigate low-wavenumber content away from the source and to generate the temporal integral of the wavefield Lagrangian at the source location.

Although the passive imaging condition in equation 13 involves autocorrelation of the displacement field $\mathbf{U}$, the correlation between the same wave modes is attenuated as shown by Rocha et al. (2016b, 2017). In contrast, at the source, the correlation between P- and S-wave modes is preserved, producing a peak amplitude directly related to the source mechanism (see Appendix A) instead of a nodal plane as the PS correlation. Therefore, the EPIC correlates different modes using the displacement field directly, without wave-mode decomposition at each extrapolation time step.

Passive imaging conditions: Extended domain

The passive imaging conditions presented above are based on zero-lag wavefield correlation; thus, they can be considered as special cases of a more general correlation-based comparison between wavefields. As discussed previously, extending wavefield correlation beyond zero lag is useful because it provides additional information, such as velocity accuracy (Sava and Vasconcelos, 2011). The temporal and spatial dependences of the wavefields allow one to compute space-lag image gathers (Rickett and Sava, 2002) and/or time-lag image gathers (Sava and Fomel, 2006). Extended imaging conditions (EICs) are also applicable to passive imaging, as shown by Witten and Shragge (2015) for extrapolated scalar wavefields.

For wave-mode decomposed elastic wavefields, we define

$$I_{\alpha_1\alpha_2}(\mathbf{x}, \boldsymbol{\lambda}, \tau) = \sum_t \alpha_1(\mathbf{x} + \boldsymbol{\lambda}, t + \tau)\alpha_2(\mathbf{x} - \boldsymbol{\lambda}, t - \tau), \quad (14)$$

where $\boldsymbol{\lambda}$ and τ are the spatial and temporal lags, respectively. Symbols α_1 and α_2 stand for either $P(\mathbf{x}, t)$ or components of $\mathbf{S}(\mathbf{x}, t)$ from equation 10; however, this can generate many possible extended images for elastic potentials when using the S-vector potential components. Exploiting the scalar S-wave energy density leads to a single extended image similar to equation 11. For EPIC (equation 13), we adapt the approach used in equation 14 to write

$$I_E^L(\mathbf{x}, \boldsymbol{\lambda}, \tau) = \sum_t [(\rho(\mathbf{x}+\boldsymbol{\lambda})\dot{\mathbf{U}}(\mathbf{x}+\boldsymbol{\lambda}, t+\tau)) \cdot (\dot{\mathbf{U}}(\mathbf{x}-\boldsymbol{\lambda}, t-\tau)) - (\underline{\underline{\mathbf{c}}}(\mathbf{x}+\boldsymbol{\lambda})\nabla\mathbf{U}(\mathbf{x}+\boldsymbol{\lambda}, t+\tau)) : (\nabla\mathbf{U}(\mathbf{x}-\boldsymbol{\lambda}, t-\tau))], \quad (15)$$

where we note that ρ and $\underline{\underline{\mathbf{c}}}$ are similarly shifted leaving the resulting image volumes asymmetric. We can also obtain the EIC for the Hamiltonian form by changing the sign between the two terms inside the brackets in equation 15.

In general, one can estimate the velocity inaccuracy on extended image gathers by evaluating the focusing quality around zero lag. The more focused the energy is around zero lag, the closer the migration velocity is to the true velocity, as shown in many cases for active source seismic wavefield tomography (Albertin et al., 2005; Yang and Sava, 2011, 2015; Diaz et al., 2013; Yang et al., 2013). More recently, Witten and Shragge (2017a, 2017b) use extended images in passive source wavefield tomography and show how calculating a single EIC at each estimated event location can assist with the elastic velocity inversion procedure. In this paper, besides evaluating the quality of the energy image with the correct velocity, we investigate the extended images for PSIC and EPIC to investigate sensitivity to velocity inaccuracy, and thereby infer potential application to the microseismic velocity estimation problem.

METHODOLOGY

Although EPIC exploits the interaction of back-propagated P- and S-direct arrivals, we need to address some caveats that arise during practical implementation of elastic time-reversal wavefield extrapolation: limited aperture and the presence of fake-mode artifacts. In general, acquired seismic data are incomplete and possibly spatially aliased, causing truncation artifacts (especially at the edges of the receiver acquisition patch) during backpropagation. Truncations are characterized with the same wave mode as the original data events, but they have different propagation directions that can cause spurious artifacts when applying EPIC. With a straightforward numerical experiment in the "Examples" section, we illustrate how the truncations create such artifacts — and we demonstrate how they can be mitigated.

A second class of elastic wavefield artifact appearing in the PS and energy images arises from partial injection of single-mode data events (i.e., processed P- or S-wave data) into the wavefield-displacement vector. This generates P- and S-wave modes regardless of their single-mode character, which are commonly called fake modes because they do not represent true data events (Yan and Sava, 2008; Ravasi and Curtis, 2013; Duan and Sava, 2015).

To mitigate both types of artifacts in the PS and energy images and obtain a better source location estimation result, we choose to first separate the P- and S-wave arrivals in the data domain and generate two elastic wavefields, one with each individual wave mode arrival. Following this approach leads to PS and energy images with wave-mode separated wavefields. Then, such images may be subtracted from the corresponding PS and energy images that use P- and S-arrivals as input to generate a final image I that is largely free of artifacts:

$$I = I^{(P,S)} - I^{(P)} - I^{(S)}, \quad (16)$$

where $I^{(P)}$ and $I^{(S)}$ are the images using P- and S-wave arrivals only as input, respectively, whereas $I^{(P,S)}$ uses both arrivals. We compute all image terms in equation 16 with the same imaging condition, either PS (I_{PS}) or energy (I_E): The superscripts with parentheses only indicate images formed with P- and/or S-data events. By following this novel approach of mitigating extrapolation-related artifacts, we

Downloaded 03/14/19 to 138.67.129.23. Redistribution subject to SEG license or copyright; see Terms of Use at http://library.seg.org/

obtain an energy image free of correlated truncation events and with attenuated fake-mode artifacts.

Separating the P- and S-wave arrivals in the multicomponent data domain is computationally inexpensive, but it does introduce a preprocessing step that requires user input in determining appropriate windowing parameters. Only one additional wavefield extrapolation is necessary, considering that we can generate wavefield $\mathbf{U}$ — from the P-arrival only — and we can generate wavefield $\mathbf{V}$ — from the S-arrival only. A third composite wavefield $\mathbf{W} = \mathbf{U} + \mathbf{V}$ is effectively equal to extrapolation using P- and S-arrivals by considering linearity of the extrapolators. Witten and Shragge (2017a) also require wave-mode separation in the data domain and two wavefield extrapolations for their acoustic passive imaging and inversion implementations. It is important to note that this data-domain separation approach would be more difficult for a swarm of microseismic events containing overlapping P- and S-wave arrivals.

3D NUMERICAL EXAMPLES

In this section, we present PS and energy images showing the estimated source position for correct constant velocity models. Then, we analyze the imprint of velocity inaccuracy on conventional and extended images. We examine the benefits of applying EPIC in a more complex 3D synthetic velocity model with realistic acquisition configuration. We conclude by applying the method to a microseismic event from a 3D field data set.

Experiment 1: Focusing with correct velocity

Our first numerical experiment investigates the imaging conditions developed above in an idealized microseismic monitoring experiment where the true velocity model is constant and known ($V_P = 3.0$ km/s and $V_S = 1.8$ km/s). In this scenario, we expect that a well-devised imaging condition should deliver a strong and focused correlation at the correct event location. Figure 1a shows the acquisition and model geometry of such an experiment, where multicomponent receivers are distributed at the surface with a realistic fixed spacing ($\Delta x = \Delta y = 0.25$ km, covering a 16 km^2 area). We locate the microseismic event at the center of the 3D model ($x = y = z = 2$ km), and we assume a double-couple stress source mechanism oriented at 45° with respect to the x-axis. For this scenario, the source-moment tensor has nonzero components of $\tau_{zz} = 1$ and $\tau_{xx} = -1$. Using a Ricker wavelet with peak frequency of 16 Hz and model grid spacing of $\Delta x = \Delta y = \Delta z = 0.01$ km, we generate 3D synthetic elastic data, followed by backpropagation and the application of the various imaging conditions.

Figure 1b and 1c shows the images obtained using the autocorrelation of the P- and S-wavefields (equations 8 and 9), respectively. In either image, the low-wavenumber content arising due to wavefield autocorrelation contaminates the whole image space (especially its shallow part), and effectively prevents an identifiable focus at the source location. Alternatively, the crosscorrelation of P- and S-wave modes (equation 11) generates the image in Figure 1d with minimal low-wavenumber content and a strong amplitude event at the correct source location. The EPIC based on the Hamiltonian operator I_E^H (Figure 1e, using equation 12) represents the total energy stacked over time, which results in a strong low-wavenumber pattern similar to those in the autocorrelation images (Figure 1b and 1c). In contrast, the EPIC based on the Lagrangian operator I_E^L (Figure 1f, using equation 13) shows a result similar to the PS image, with a strong and focused correlation at the source location. In all images, one should

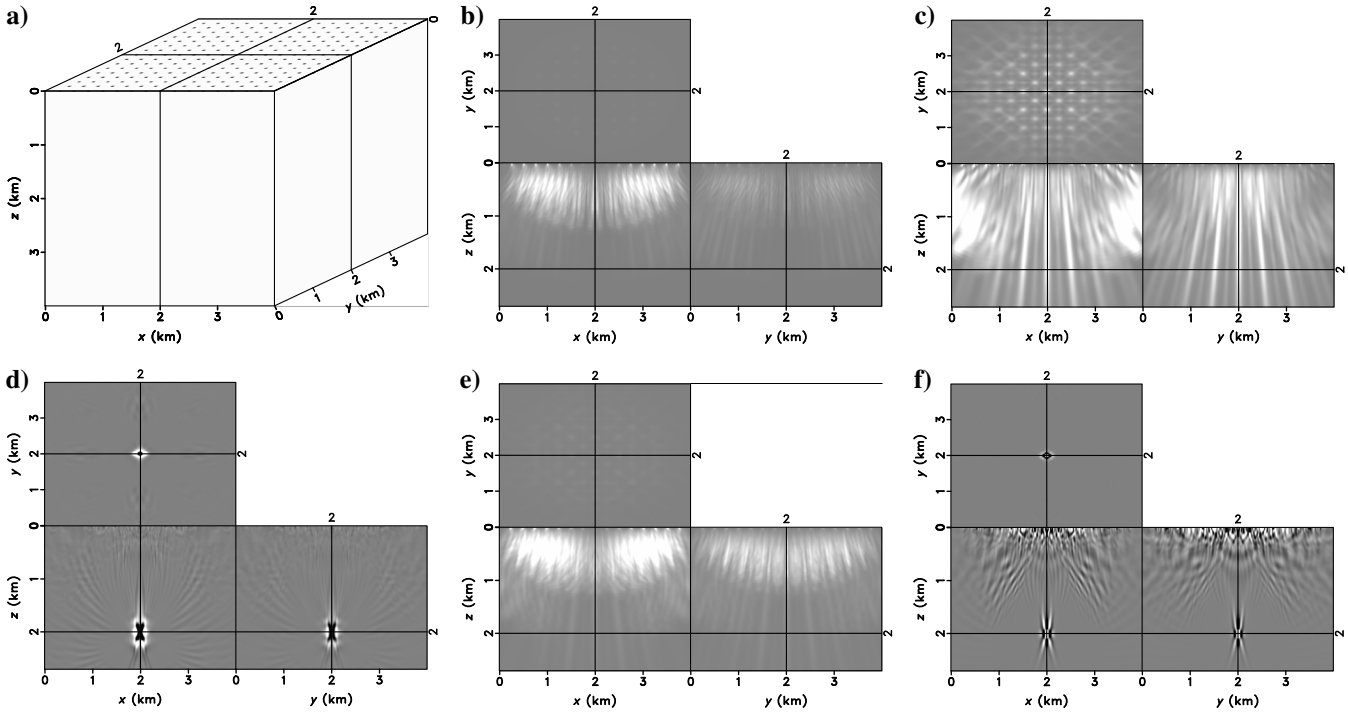


Figure 1. Constant-velocity experiment that consists of (a) an earth model with $4 \times 4 \times 4$ km and multicomponent receivers (black dots) spaced by 0.25 km at the surface. (b) PP, (c) SS, (d) PS and energy images using equations 12e and 13f. The PS and energy images have strong and focused peaks at the source location compared with all other images that exhibit strong low-wavenumber artifacts.

Downloaded 03/14/19 to 138.67.129.23. Redistribution subject to SEG license or copyright; see Terms of Use at http://library.seg.org/

consider smearing and truncation artifacts when estimating a source location using wavefield imaging methods for passive seismic because sparse and band-limited data acquisition prevents extrapolated waves from collapsing into an idealized focus.

To obtain all images in Figure 1, we use the procedure explained in the methodology section, i.e., computing three separated energy images, such as $I = I^{(P,S)} - I^{(P)} - I^{(S)}$. This is necessary because truncation events correlate with the true events and create a strong artifact at the center of the energy image. Figure 2a and 2b shows schematic representations of the truncation wavefronts away and close to the source location, respectively. In Figure 2c, we show the vertical component of the back-propagated elastic wavefield at a snapshot prior to events focusing at the source location. Besides the true wave events (P- and S-back-propagated microseismic arrivals), truncations exist and interact with the true events close to the focusing location and time. Note how the S-wave truncations interfere with themselves and with the incoming P-wave event. In addition, the fake P-wave mode also appears strong in Figure 2c, but generates artifacts mostly in the shallow area (down to 1 km in depth). Figure 2d shows the same energy image as in Figure 1f, but without the subtraction of such imaging artifacts. We note residual low-wavenumber content and the different correlation at the source in Figure 2d as compared with Figure 1f. This experiment in a constant-velocity medium demonstrates how (1) low-wavenumber artifacts from wavefield autocorrelation impede a visual interpretation of the source location, (2) truncation events substantially alter the imaged events, and (3) imaging conditions that exploit different wave modes in the displacement field localize the source by producing a focused correlated event at the true source position, especially for EPIC, which produces a focused peak at the source location.

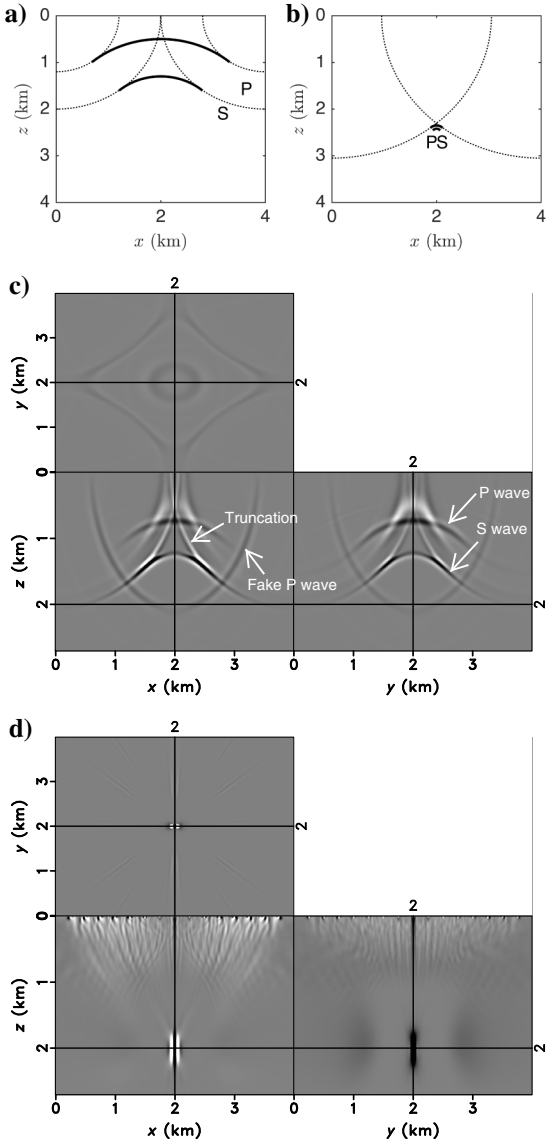


Figure 2. Schematic representation of (a) P- and S-waves back propagated with truncation events (dashed lines). Close to their focus points, (b) P- and S-waves correlate with their respective truncation events, which have the polarity of their original wave but different propagation directions. (c) Snapshot of the vertical component from the back-propagated elastic wavefield. As indicated by the arrows, note the true back-propagated events and the associated artificial extrapolated events. (d) Energy image with the strong artifact caused by the truncation, as opposed to the energy image without such artifact (Figure 1f).

Experiment 2: Sensitivity to changes in velocity and extended images

Our second experiment investigates the sensitivity of the different imaging conditions when using the incorrect velocity. We expect that the correlation between P- and S-waves occurs at a different location and time than for the correct model scenarios; however, we would still expect a coherent pattern useful for interpretation and migration velocity analysis. In Figures 3 and 4, we compute the PS and energy images for different velocities using the same experimental setup as in Figure 1. We create incorrect constant velocities by globally increasing or decreasing the original velocities by 8%. For improved visualization, we show magnified slices from the original image volumes. The images exhibit misfocusing due to the incorrect velocities, and they show a correlation point either too shallow or too deep with respect to the correct source location. We note that all PS images have a zero crossing at the point of maximum correlation (e.g., at $x = y = z = 2$ km in Figure 3e). Though present in experiment 1, but more noticeable here, the use of the absolute value of the S-vector potential creates zero-crossing patterns throughout the images due to the existence of nodal planes. However, for energy images computed with incorrect velocities (Figure 4), we observe a more straightforward and interpretable moveout pattern from the unfocused events relative to the PS images because of their fewer side lobes, as well as an absence of visible nodal planes. This misfocusing of event images for incorrect velocities is important in the context of assessing velocity and source location errors.

We also compute extended images with correct and incorrect velocities for PSIC (Figure 5) and EPIC (Figure 6). These extended image examples are generated with the same incorrect velocities and displayed similarly to Figures 3 and 4. For simplicity, we evaluate these extended images at a single spatial point located at the correct source position and with spatial lags only (with axes $\lambda_x, \lambda_y, \lambda_z$), thus generating the 3D volumes shown in Figures 5 and 6. As discussed above, we expect to observe unfocused events in the extended domain when velocities are incorrect, and a focused event at zero lag when P- and S-wave velocities are correct. Indeed, we note that these misfocusing attributes exist in the extended domain for both imaging conditions, but they are expressed

differently. Compared with the extended PS image, the energy one shows significantly fewer lobes and no nodal planes; therefore, exhibits imaged waveforms more straightforward to interpret. However, whereas the extended energy image exhibits symmetric unfocused events with respect to the λ_z-axis, the extended PS image shows a single unfocused event either at positive or negative λ_z values. This indicates that, although the events in the extended energy image exhibit more straightforward waveforms, interpreting the direction of the required velocity update (either positive or negative) is more challenging. For instance, by looking at the extended energy images when we perturb only the S-wave velocity by $-\%8$ or $+\%8$ (Figure 6d and 6f), we note a similar dislocation from zero lag but different focusing attributes. Therefore, the extended energy image correctly provides the magnitude of the velocity perturbation, but apparently it has lower sensitivity with respect to the perturbation sign. Based on such differing sensitivity, we infer that the two EICs would provide complementary information for microseismic migration velocity analysis.

Experiment 3: SEG/EAGE 3D overthrust model

Our third numerical test investigates how PSIC and EPIC compare using a more complex velocity model — SEG/EAGE 3D overthrust (Aminzadeh et al., 1994). We place the source at the center of the model ($x = y = 3.048$ km, $z = 1.073$ km in Figure 7a), and use a nonuniform distribution of 192 multicomponent receivers at elevations ranging between $z = -213$ and -423 m (Figure 7c). These receiver coordinates mimic the acquisition geometry of the following field data example. Because the original 3D overthrust model contains only the P-wave velocity, we arbitrarily create an S-wave velocity model using an oscillatory PS velocity ratio as a function of depth (Figure 7b). We model and extract synthetic data at the 192 receiver locations, and we compare the PS and energy images using a source mechanism different from the previous two numerical experiments. The corresponding source-moment tensor has nonzero components of $\tau_{zz} = 1$, $\tau_{yy} = -2$, and $\tau_{xx} = 1$.

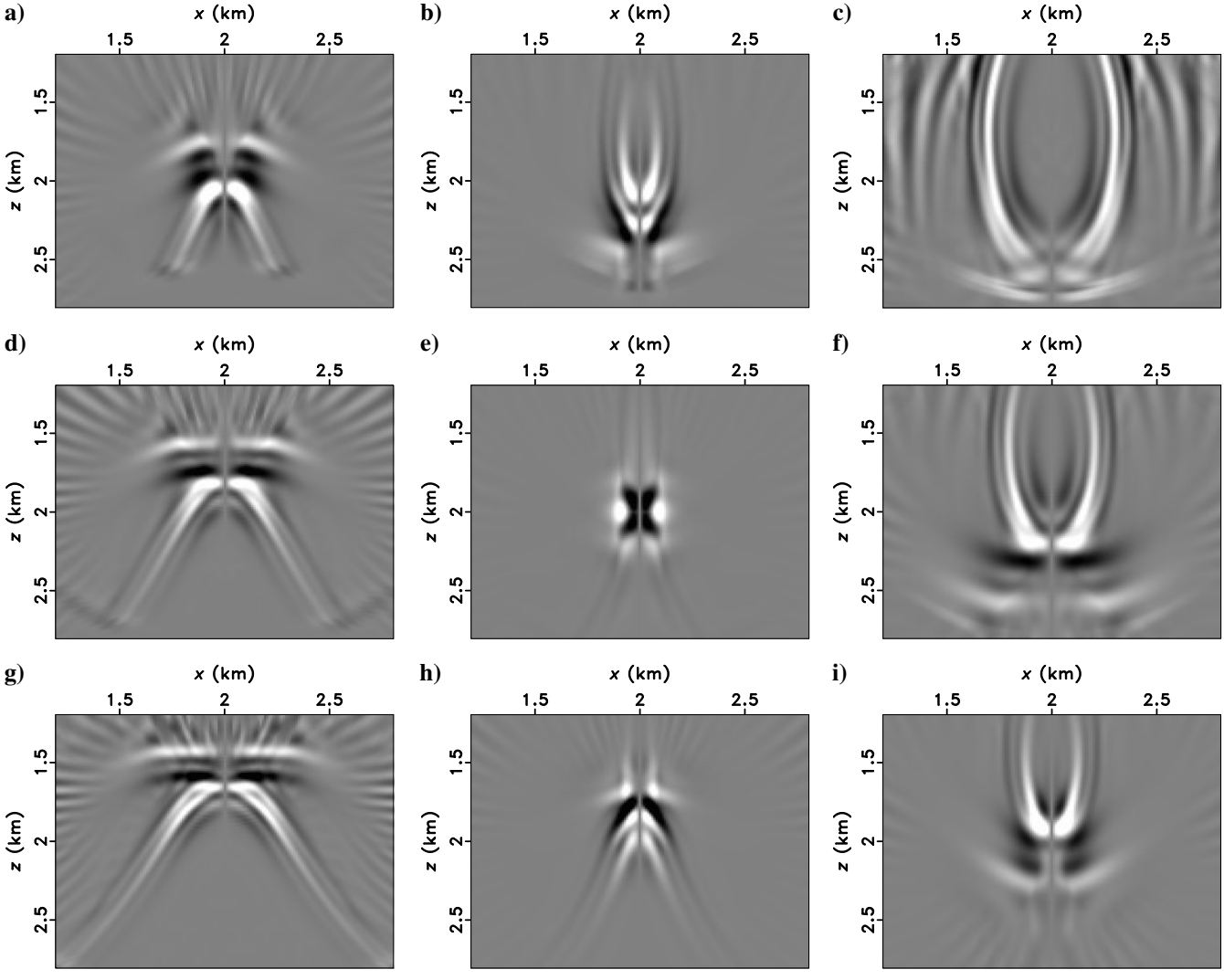


Figure 3. PS images with incorrect velocities with respect to a $V_P = 3.0$ km/s and $V_S = 1.8$ km/s. The top, middle, and bottom rows correspond to -8%, 0%, $+8\%$ changes in the P-wave velocity; and the left, middle, and right columns correspond to -8%, 0%, $+8\%$ changes in the S-wave velocity. Note that the unfocused events with respect to the focused correlation in the central image (which uses the correct velocity).

Downloaded 03/14/19 to 138.67.129.23. Redistribution subject to SEG license or copyright; see Terms of Use at http://library.seg.org/

Downloaded 03/14/19 to 138.67.129.23. Redistribution subject to SEG license or copyright; see Terms of Use at http://library.seg.org/

Figure 8 shows the PS and energy images for this numerical experiment. Figure 8a and 8b shows the entire image volumes, whereas Figure 8c and 8d magnifies around the source location. Originally, the PS and energy images have strong artifacts in the shallow subsurface due to the aforementioned caveats (i.e., truncated acquisition, nonexistent modes created by displacement injection) from elastic wavefield extrapolation; however, by applying a straightforward exponential gain with depth to both images to mitigate these effects, we obtain the images shown in Figure 8a and 8b. The image locations colored in red represent clipped colorbar amplitudes, and they are generally consistent with the estimated source locations for both images (Figure 8c and 8d). The PS image (Figure 8c) exhibits the clipped amplitudes approximately 200 m away from the source location, mainly due to the zero crossing that occurs at the known source location. Meanwhile, the energy image (Figure 8d) has the clipped amplitudes within one grid cell of the true source location. Therefore, by comparing the magnified images in Figure 8c and 8d, we observe more consistent focusing of the energy image relative to the PS image, and the misplacement of the clipped peak amplitude for the PS image. As discussed in the theory section, data preprocessing could handle polarization issues with the PS correlation, but potentially at the cost of a lower resolution image.

To observe focusing in the extended domain, we generate extended images for both imaging conditions using the correct velocity only (Figure 8e and 8f). As previously, the extended PS image has a nodal plane at zero lag and exhibits substantial defocusing away from zero lag even though the velocities are exact. The extended energy image shows a more focused event at zero lag without nodal planes. The $\lambda_x - \lambda_y$ plane of the energy image in Figure 8f might suggest that the source has its primary stress component in the y-axis due to the elongation direction of the imaged event. However, validating a direct extraction of the source mechanism warrants further research beyond the scope of this paper.

The SEG/EAGE 3D overthrust experiment demonstrates that the direct correlation between Helmholtz decomposed P- and S-wavefields produces strong imaging artifacts with amplitudes surpassing the correlation at the true source position. EPIC involves an indirect

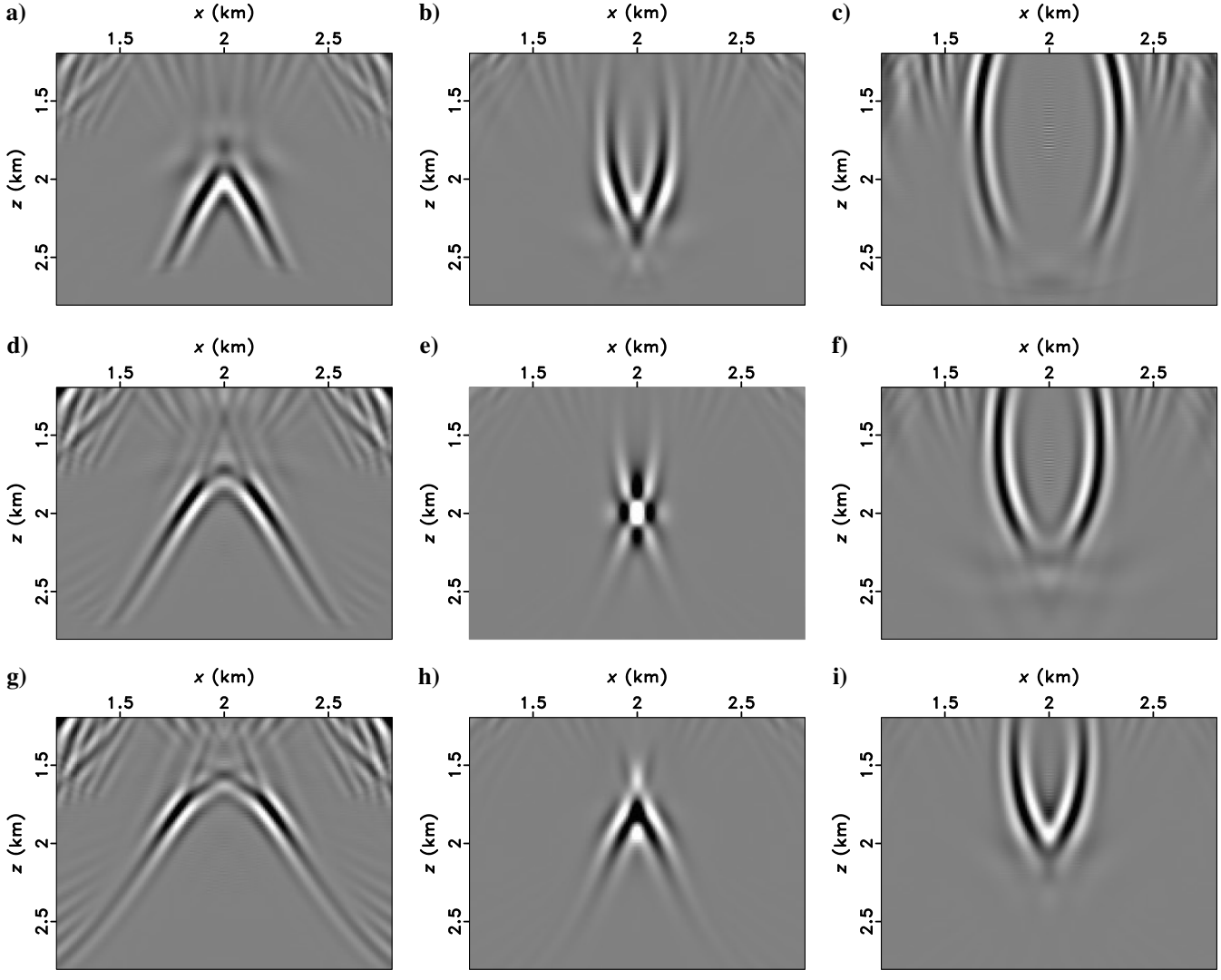


Figure 4. Energy images with incorrect velocities, computed and displayed as in Figure 3. Compared with the PS images in Figure 3, the energy correlation produces unfocused imaged events that are more straightforward to interpret and without zero crossings.

correlation of P- and S-waves that produces a stronger correlation at the source location compared with the imaging artifacts, in the conventional and extended domains. The difference between PSIC and EPIC becomes more evident with the increasing model complexity.

Experiment 4: Field-data example

The final experiment uses microseismic field data recorded by a passive seismic acquisition campaign during a hydraulic stimulation program in eastern Ohio, USA. Witten and Shragge (2017b) present a thorough description of the experiment, data set and subsequent preprocessing. The receiver array consists of 192 multicomponent (3C) geophones, whose geometry is shown in Figure 7c. We use P- and S-wave velocity models (Figure 9) obtained by the image-domain velocity inversion described in Witten and Shragge (2017b). From a data catalog of 28 high-S/N microseismic events, we select one microseismic event (single P- and S-arrivals) of magnitude $M_w = 0.24$. The processing applied prior to backpropagation and imaging involves different steps compared with the acoustic implementation from Witten and Shragge (2017b): (1) rotating the northing and easting components to the x-, y-components consistent with the velocity model geometry (by an angle of 41°), (2) applying a band-pass filter from 4 to 30 Hz (with no trace normalization, nor application of an envelope filter), and (3) implementing stronger weighting of early P- and S-wave arrivals. Figure 10 shows the multicomponent data set processed using such an approach.

We inject the microseismic event shown in Figure 10 into the velocity model (Figure 9), and we apply PSIC and EPIC. We use the same image subtraction procedure ($I = I^{(P,S)} - I^{(P)} - I^{(S)}$) and exponential gain with depth as in experiment 3. Figure 11 presents the final results of the imaging procedure. Because in this field data set example, we do not know the true source location, we elect to present image slices corresponding to the point of maximum amplitude for each imaging condition clipped using the same

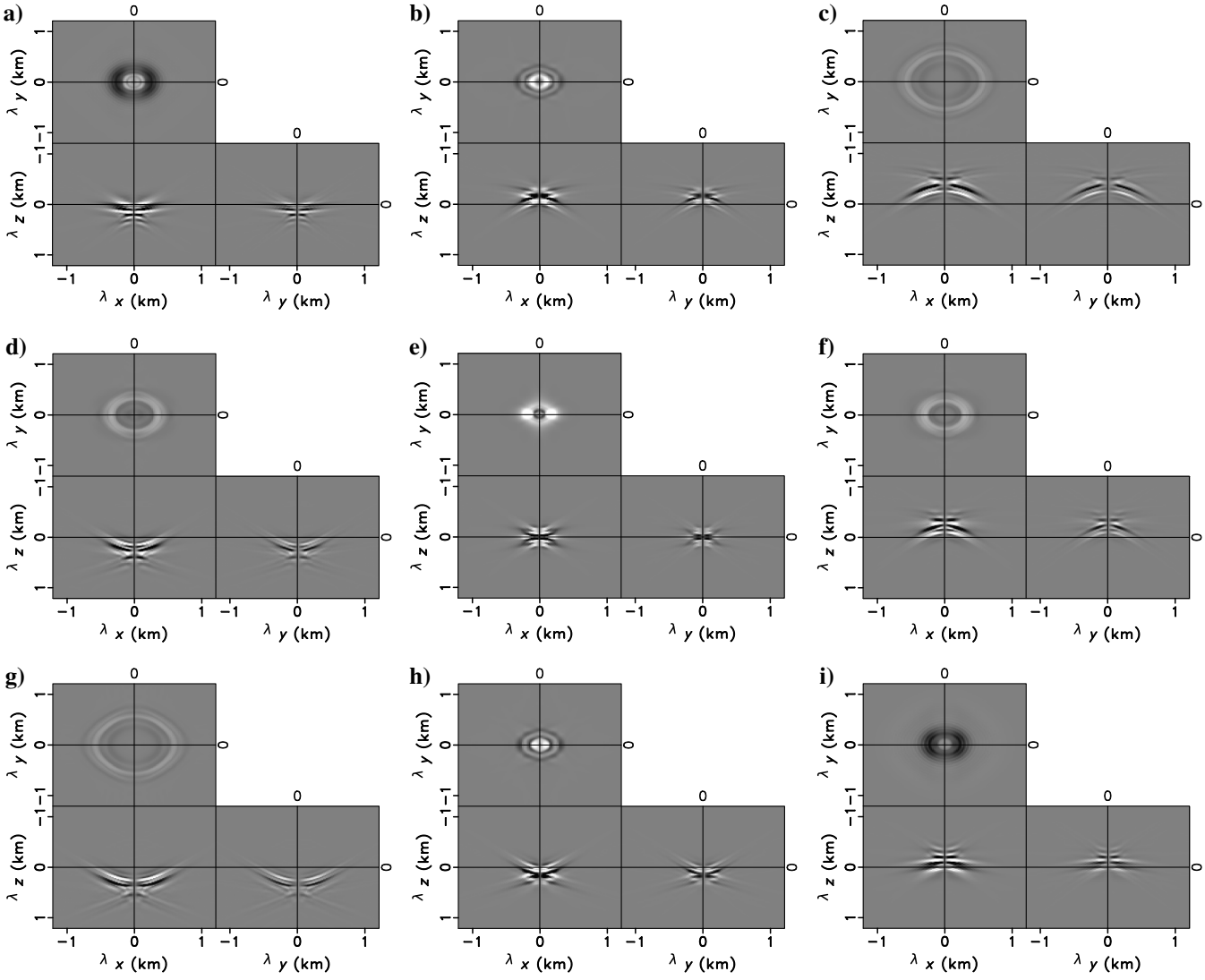


Figure 5. Extended PS images with incorrect velocities. The top, middle, and bottom rows correspond to −8%, 0%, +8% changes in the P-wave velocity; and the left, middle, and right columns correspond to −8%, 0%, +8% changes in the S-wave velocity. Note the unfocused events with respect to the focused correlation in the central image (which uses the correct velocity).

Downloaded 03/14/19 to 138.67.129.23. Redistribution subject to SEG license or copyright; see Terms of Use at http://library.seg.org/

Downloaded 03/14/19 to 138.67.129.23. Redistribution subject to SEG license or copyright; see Terms of Use at http://library.seg.org/

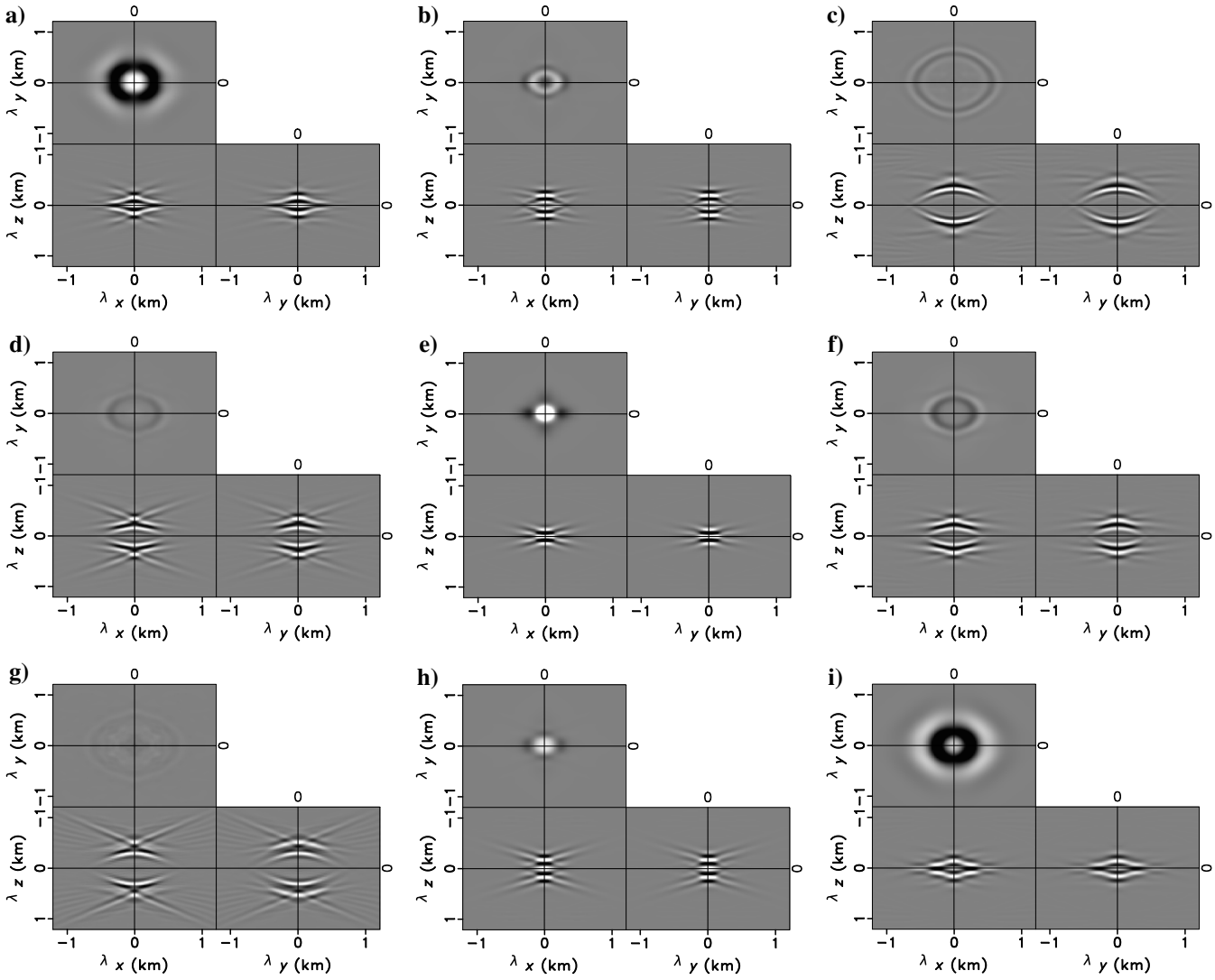


Figure 6. Extended energy images with incorrect velocities, organized similarly to Figure 5. Compared with the PS images in Figure 5, the energy correlation produces unfocused images that are more straightforward to interpret, are symmetric with respect to the λ_z-axis, and contain no zero crossings.

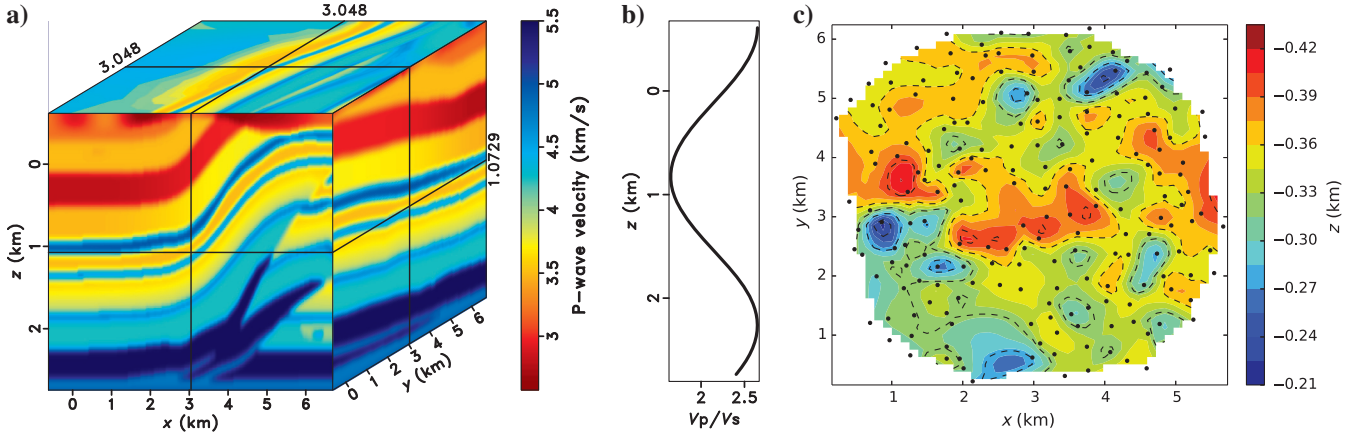


Figure 7. SEG/EAGE overthrust experiment: (a) P-wave velocity from the 3D overthrust model and (b) PS velocity ratio. (c) Receiver coordinates used for the overthrust and field-acquisition experiments shown in Figures 9 and 11.

Downloaded 03/14/19 to 138.67.129.23. Redistribution subject to SEG license or copyright; see Terms of Use at http://library.seg.org/

percentile (Figure 11a and 11b). As observed in the image slices, the discrepancy between the estimated PS and energy source locations is $[\Delta x, \Delta y, \Delta z] = [366, 146, 91]$ m. The PS image in Figure 11a exhibits more artifacts away from its presumed source location (especially on the x-y plane) when compared with the energy image in Figure 11b. Looking at the magnified images (Figure 11c and 11d), we note a further advantage of the energy image relative to the PS image: Most of the correlated energy is positive. Finally, the extended energy image (Figure 11f) exhibits a more centralized focus around zero lag when compared with the extended PS image (Figure 11e). Although there is residual energy beyond zero lag, both extended images indicate that the provided velocities obtained by image-domain tomographic inversion are sufficiently consistent and, therefore, are accurate by the self-consistency principle (Witten and Shragge, 2017a). Overall, the field-data example demonstrates that EPIC behaves well in the presence of noise, realistic acquisition geometry, as well as possible residual errors in the velocity models. This experiment also illustrates that elastic wavefield imaging methods are more effective

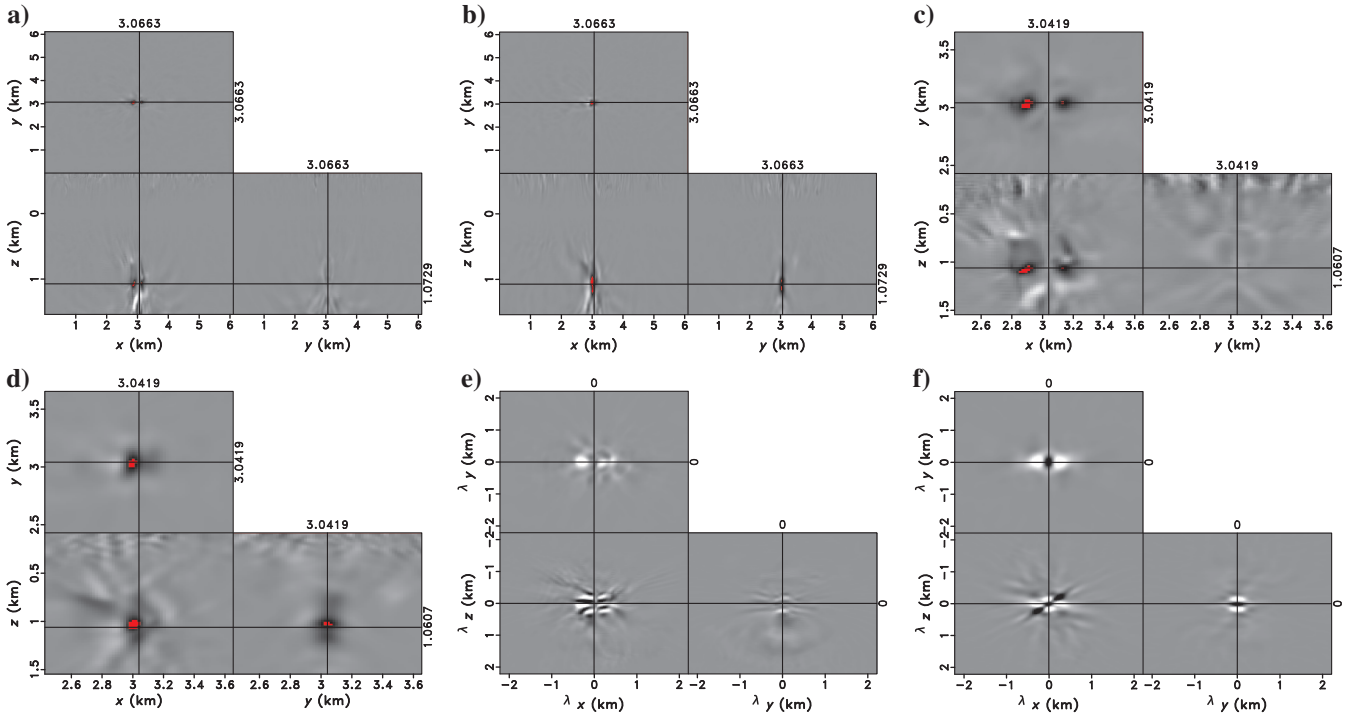


Figure 8. SEG/EAGE overthrust experiment: (a) PS and (b) energy images for a stress source with $\tau_{xx} = -2, \tau_{yy} = 1, \tau_{zz} = 1$. Magnified (c) PS and (d) energy images, as well as extended (e) PS and (f) energy images. The energy correlation exhibits peak amplitudes (in red) that are closer to the source location in (d) when compared with (c), and are more focused in the extended domain in (f) when compared with (e).

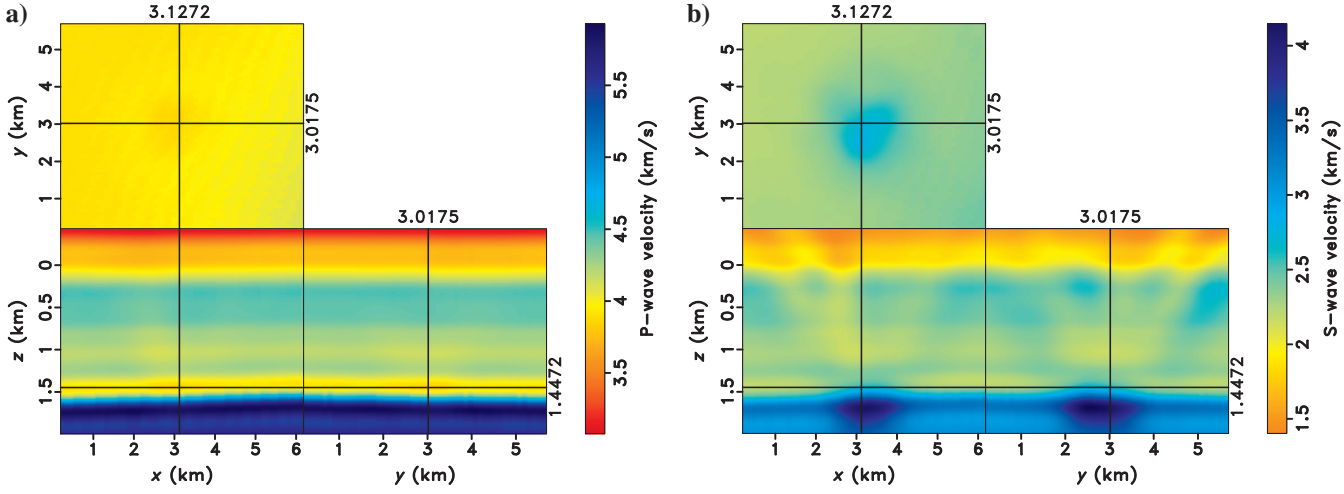


Figure 9. Field-data experiment: (a) P- and (b) S-wave velocity models.

Downloaded 03/14/19 to 138.67.129.23. Redistribution subject to SEG license or copyright; see Terms of Use at http://library.seg.org/

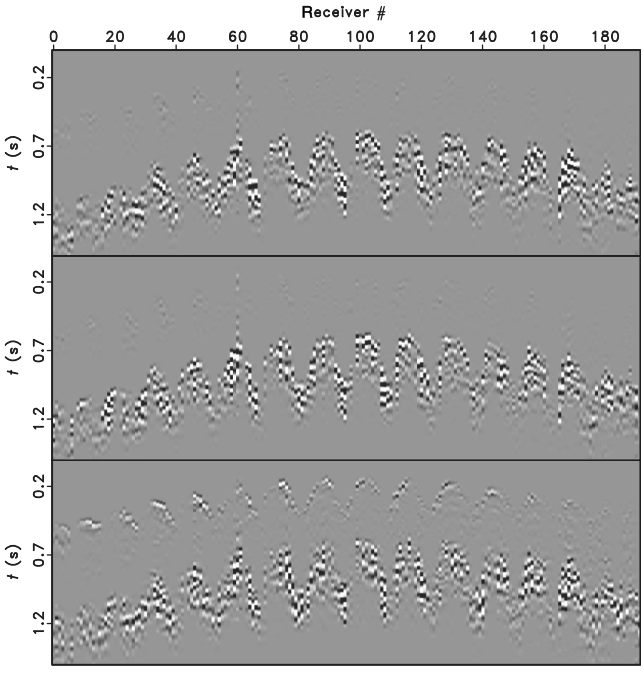


Figure 10. Field-data experiment: x (top), y (middle), and z (bottom) components from the processed data set containing a single microseismic event. Note the P- (from $t = 0$ to 0.6 s) and S- (from $t = 0.6$ to 1.5 s) arrivals, and how the P-wave arrival is stronger in the vertical (z) component.

for real surface passive seismic with relatively dense receiver geometry, after the complementary image provided by the energy correlation.

DISCUSSION

Based on the numerical examples presented in this paper, EPIC not only serves as an alternative procedure for obtaining source location estimates and examining velocity accuracy, but it also offers some improvements relative to conventional PSIC. The more directly interpretable images obtained by the proposed imaging condition not only reduce uncertainty of the event location, but they also help with velocity estimation based on migration velocity analysis methodology (i.e., the semblance principle). This interpretational simplicity is due to the absence of nodal planes and associated polarity changes, which are ubiquitous in PS correlation. The penalty function commonly used in image-domain wavefield tomography (Symes and Carazzone, 1991; Mulder and ten Kroode, 2002; Yang and Sava, 2015; Witten and Shragge, 2017a) requires extended-domain images with fewer artifacts and better delineated events. In the context of passive imaging and inversion, our examples show that such characteristics are enhanced by the energy correlation. However, computing tomographic velocity updates requires reliable gradient magnitude and direction information, and the latter appears to not be sufficiently distinguishable by the energy correlation alone. In addition, for both imaging conditions, differentiating between P- and S-wave velocity inaccuracies is only possible with complementary information from autocorrelation P- and S-wave imaging

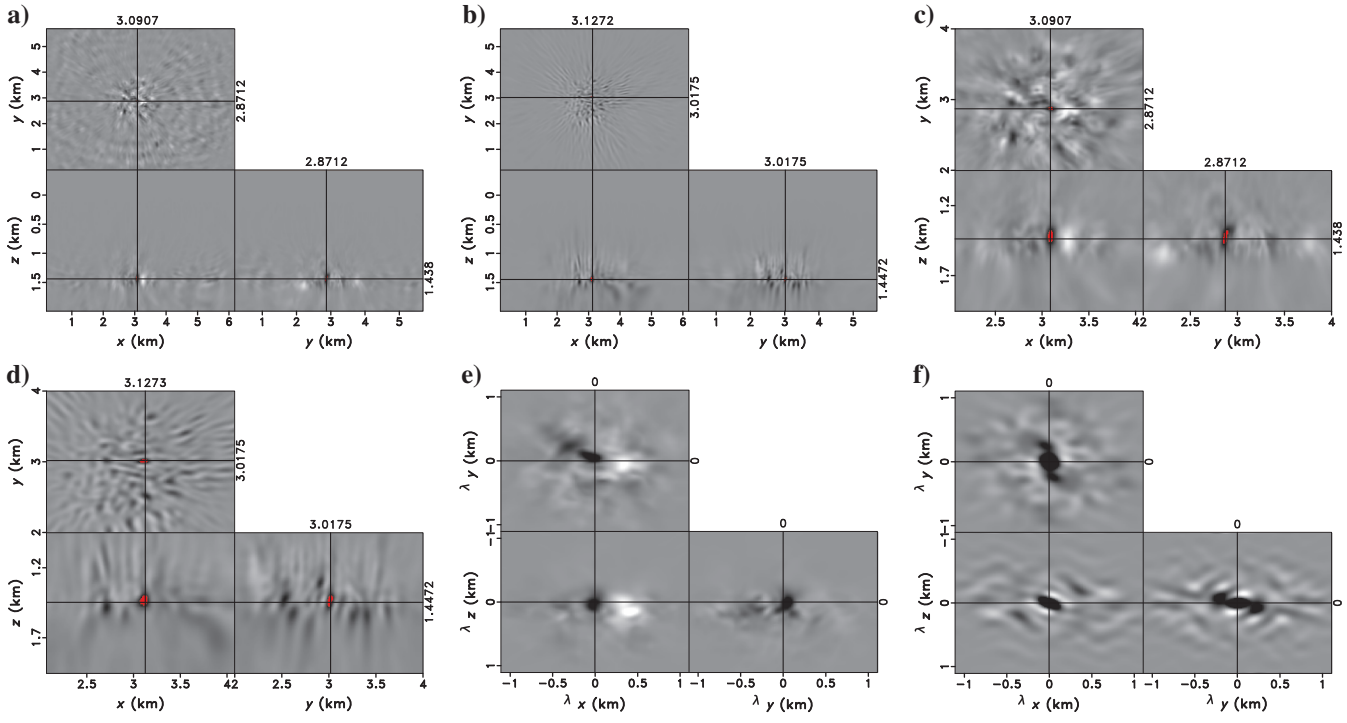


Figure 11. Field-data experiment: (a) PS and (b) energy images for the field data set. Magnified (c) PS and (d) energy images, as well as extended (e) PS and (f) energy images. The energy correlation has peak amplitudes (in red) that are closer to the source location in (d) when compared with (c), and are more centralized in the extended domain in (f) when compared with (e).

Downloaded 03/14/19 to 138.67.129.23. Redistribution subject to SEG license or copyright; see Terms of Use at http://library.seg.org/

conditions, as shown previously in Witten and Shragge (2017a). Thus, it is our view that these various EICs could play a complementary — but important — role in applications of microseismic migration velocity analysis.

The fact that the energy correlation formalism introduced above is able to handle anisotropy is not demonstrated here; however, the pathway for incorporating anisotropy should be clear based on the theory presented in this paper. Current wave-mode decomposition methods during wavefield extrapolation for anisotropic media remain computationally intensive (Zhang and McMechan, 2010; Yan and Sava, 2011; Cheng and Fomel, 2014; Sripanich et al., 2015; Wang et al., 2016; Rocha et al., 2017). Until these methods become more efficient, the energy correlation serves as a formal and cost-effective method for correlating different wave modes for anisotropic elastic passive imaging. Our imaging condition does not add a significant computational burden because it requires the same spatial derivatives as those in Helmholtz decomposition and straightforward temporal derivatives (identical to those computed at each elastic extrapolation time step). Moreover, the extended energy image is sufficiently computed at a single common image point for migration velocity analysis (Witten and Shragge, 2017a).

We also advocate the usage of elastic wavefield extrapolation as opposed to acoustic extrapolation, which is applied to the same field data set in a related paper (Witten and Shragge, 2017b). Acoustic time-reversal involves normalization of each individual trace and computing the complex envelope of the seismic signals, thereby altering the amplitude and phase of the acquired signals. Although essential for acoustic velocity analysis, such a procedure undermines any possible cotemporal radiation pattern analysis (i.e., through joint microseismic velocity analysis and moment-tensor inversion). Acoustic extrapolation assumes single-component data and, therefore, does not exploit the polarization of seismic waves. Elastic extrapolation does not involve these issues and offers finer imaging sampling considering the same frequency band from data. However, it remains substantially more expensive than its acoustic counterpart especially for 3D models, though it is achievable at the scale of a small cluster or even a high-end workstation when using graphics processing unit-based 3D elastic propagators (Weiss and Shragge, 2013).

CONCLUSION

For passive wavefield imaging with surface-recorded multicomponent data, EPIC offers an elegant solution for locating seismic sources within an arbitrary earth model. Based on energy conservation for extrapolated wavefields, our imaging condition represents the temporal integral of the Lagrangian operator (which is the difference between kinetic and potential wavefield energy terms) and produces an image that is theoretically related to the source mechanism. For simple models, we demonstrate that the energy image exhibits better attributes than PS images in terms of image quality and velocity sensitivity. For more realistic synthetic and field-data examples, the improved results from applying EPIC are similarly illustrated despite the introduction of field data noise, sparser and nonuniform receiver geometry, and more complex earth models. We assert that the preclusion of wave-mode decomposition during extrapolation in our method permits its implementation to anisotropic earth models without substantial additional cost or complication, as opposed to the conventional PSIC that generally relies on Helmholtz decomposition.

In summary, we have validated the five advantages stated in the "Introduction" section: (1) handling radiation patterns without the generation of nodal planes, (2) producing a peak amplitude at the source location, (3) precluding wave-mode decomposition at each time step, (4) downweighting identical wave modes and enhancing distinct ones during correlation, and (5) offering complementary extended image attributes for migration velocity analysis. Future work involves exploring the further benefits of EPIC for anisotropic media, potential inferences on focal mechanism and its inversion, and the development of a microseismic migration velocity inversion framework using the unfocused energy on extended image gathers.

ACKNOWLEDGMENTS

We thank the sponsors of the Center for Wave Phenomena, whose support made this research possible. We thank Statoil USA for allowing publication and ESG/Spectraseis for delivering the field data set. We acknowledge Ivan Lim Chen Ning, Paul Fowler and Roel Snieder for helpful discussions, and Yuting Duan for sharing her wavefield modeling codes. The reproducible numeric examples in this paper use the Madagascar open-source software package (Fomel et al., 2013) freely available from http://www.ahay.org.

DATA AND MATERIALS AVAILABILITY

Data associated with this research are available and can be obtained by contacting the corresponding author.

APPENDIX A

HAMILTON'S PRINCIPLE

Considering a displacement field $\mathbf{U}(\mathbf{x},t)$, the Lagrangian density function is (Ben-Menahem and Singh, 1981)

$$\mathcal{L}(\mathbf{U},\mathbf{x},t)=\frac{1}{2}\rho\|\dot{\mathbf{U}}\|^2-\frac{1}{2}(\underline{\underline{\mathbf{c}}}\nabla\mathbf{U}):\nabla\mathbf{U}. \tag{A-1}$$

The first and second terms in the Lagrangian function represent the kinetic and potential energies of the wavefield, respectively. In a medium with no external forces, the action is defined as the Lagrangian density function integrated over time

$$A(\mathbf{U})=\int_0^T\mathcal{L}(\mathbf{U},t)\mathrm{d}t. \tag{A-2}$$

Hamilton's variational principle states that the action is stationary under small displacements, and can be expressed as (Slawinski, 2003)

$$\delta A(\mathbf{U},\mathbf{x})=\delta\int_0^T\mathcal{L}(\mathbf{U},t)\mathrm{d}t=0, \tag{A-3}$$

where δ indicates the variation of a function. The variation is permutable with a definite integral and can be defined with respect to the displacement variable (Lanczos, 1970). Hence

$$\begin{aligned}\delta A(\mathbf{U},\mathbf{x})&=\int_0^T\delta\mathcal{L}(\mathbf{U},t)\mathrm{d}t\\&=\int_0^T[\mathcal{L}(\mathbf{U}+\delta\mathbf{U},t)-\mathcal{L}(\mathbf{U},t)]\mathrm{d}t=0,\end{aligned} \tag{A-4}$$

Downloaded 03/14/19 to 138.67.129.23. Redistribution subject to SEG license or copyright; see Terms of Use at http://library.seg.org/

where $\delta\mathbf{U}(\mathbf{x},t)$ is a small displacement satisfying $\delta\mathbf{U}(\mathbf{x},t=0)=\delta\mathbf{U}(\mathbf{x},t=T)=0$.

We can characterize the Lagrangian, $\mathcal{L}(\mathbf{U},t)$, for a particle at rest from $t=0$ to $t=T$, i.e., $\mathbf{U}=0$, for $0\le t\le T$. We can consider the displacement field acting on this particular point as a small perturbance to the particle at the rest. Therefore

$$\delta A(\mathbf{U},\mathbf{x})=\int_0^T \mathcal{L}(\delta\mathbf{U},t)\mathrm{d}t=0. \tag{A-5}$$

This implies that, in the absence of external work from sources and in the presence of small displacements, the energy imaging condition defined as the integral of the Lagrangian density function is zero.

In a volume V that contains sources, the action is defined as (Yu, 1964)

$$A(\mathbf{U},\mathbf{x})=\int_0^T\int_V[\mathcal{L}(\mathbf{U},t)\mathrm{d}V+W]\mathrm{d}t, \tag{A-6}$$

where the external work W is

$$W=\int_V \rho\mathbf{F}\cdot\mathbf{U}\mathrm{d}V+\int_S(\underline{\mathbf{t}}\cdot\mathbf{U})\cdot\mathbf{n}\mathrm{d}S, \tag{A-7}$$

where $\mathbf{F}(\mathbf{x},t)$ represents a body force field and $\underline{\mathbf{t}}(\mathbf{x},t)$ an external stress field acting on the surface of the considered volume. Applying the variational operator on equation A-7 and using the divergence theorem, we obtain

$$\delta W=\int_V[\rho\mathbf{F}\cdot\delta\mathbf{U}+\nabla\cdot(\underline{\mathbf{t}}\cdot\delta\mathbf{U})]\mathrm{d}V. \tag{A-8}$$

Applying the variation operator on equation A-6 and using equation A-8 leads to

$$\delta A(\mathbf{U},\mathbf{x})=\int_0^T\int_V[\mathcal{L}(\delta\mathbf{U},t)+\rho\mathbf{F}\cdot\delta\mathbf{U}+\nabla\cdot(\underline{\mathbf{t}}\cdot\delta\mathbf{U})]\mathrm{d}V\mathrm{d}t=0. \tag{A-9}$$

We consider a sufficiently small volume, such that it contains only one discrete point. In a point where either a displacement or a stress source exists, equation A-9 suggests that the energy imaging condition (defined as the integral of the Lagrangian density function) is equivalent to the action of existing sources

$$I_{\mathrm{EN}}(\mathbf{x})=\int_0^T\mathcal{L}(\delta\mathbf{U},t)\mathrm{d}t=-\int_0^T\rho\mathbf{F}\cdot\delta\mathbf{U}+\nabla\cdot(\underline{\mathbf{t}}\cdot\delta\mathbf{U})\mathrm{d}t. \tag{A-10}$$

The energy imaging, for waves generated by a displacement point force, becomes

$$I_{\mathrm{EN}}(\mathbf{x})=\int_0^T\mathcal{L}(\delta\mathbf{U},t)\mathrm{d}t=-\int_0^T\rho\mathbf{F}\cdot\delta\mathbf{U}\mathrm{d}t, \tag{A-11}$$

and by a stress source, generally described as a double couple system of forces, becomes

$$I_{\mathrm{EN}}(\mathbf{x})=\int_0^T\mathcal{L}(\delta\mathbf{U},t)\mathrm{d}t=-\int_0^T\nabla\cdot(\underline{\mathbf{t}}\cdot\delta\mathbf{U})\mathrm{d}t. \tag{A-12}$$

REFERENCES

Aki, K., and P. G. Richards, 2002, Quantitative seismology, 2nd ed.: University Science Books.

Albertin, U., P. Sava, J. Etgen, and M. Maharramov, 2005, Adjoint wave-equation velocity analysis: 75th Annual International Meeting, SEG, Expanded Abstracts, 3345–3349, doi: 10.1190/1.2370226.

Alford, R. M., 1986, Shear data in the presence of azimuthal anisotropy: 56th Annual International Meeting, SEG, Expanded Abstracts, 476–479, doi: 10.1190/1.1893036.

Aminzadeh, F., N. Burkhard, L. Nicoletis, F. Rocca, and K. Wyatt, 1994, SEG/EAEG 3-D modeling project: 2nd update: The Leading Edge, **13**, 949–952, doi: 10.1190/1.1437054.

Artman, B., I. Podladtchikov, and B. Witten, 2010, Source location using time-reverse imaging: Geophysical Prospecting, **58**, 861–873, doi: 10.1111/j.1365-2478.2010.00911.x.

Ay, E., H. S. Kuleli, F. Song, and M. N. Toksöz, 2012, Detection and enhancement of microseismic signals with correlation operators: Cross product and master event methods: International Geophysical Conference and Oil and Gas Exhibition, 561–564.

Baker, T., R. Granat, and R. W. Clayton, 2005, Real-time earthquake location using Kirchhoff reconstruction: Bulletin of the Seismological Society of America, **95**, 699–707, doi: 10.1785/0120040123.

Bazargani, F., and R. Snieder, 2016, Optimal source imaging in elastic media: Geophysical Journal International, **204**, 1134–1147, doi: 10.1093/gji/ggv494.

Behura, J., F. Forghani, and F. Bazargani, 2013, Improving microseismic imaging: Role of acquisition, velocity model, and imaging condition: 83rd Annual International Meeting, SEG, Expanded Abstracts, 2119–2123, doi: 10.1190/segam2013-1073.1.

Ben-Menahem, A., and S. J. Singh, 1981, Seismic waves and sources: Springer-Verlag.

Blias, E., and V. Grechka, 2013, Analytic solutions to the joint estimation of microseismic event locations and effective velocity model: Geophysics, **78**, no. 3, KS51–KS61, doi: 10.1190/geo2012-0517.1.

Cheng, J., and S. Fomel, 2014, Fast algorithms for elastic-wave-mode separation and vector decomposition using low-rank approximation for anisotropic media: Geophysics, **79**, no. 4, C97–C110, doi: 10.1190/geo2014-0032.1.

Crampin, S., 1985, Evaluation of anisotropy by shear-wave splitting: Geophysics, **50**, 142–152, doi: 10.1190/1.1441824.

Dellinger, J., and J. Etgen, 1990, Wave-field separation in two-dimensional anisotropic media: Geophysics, **55**, 914–919, doi: 10.1190/1.1442906.

Diaz, E., P. Sava, and T. Yang, 2013, Data-domain and image-domain wave-field tomography: The Leading Edge, **32**, 1064–1072, doi: 10.1190/tle32091064.1.

Douma, J., and R. Snieder, 2015, Focussing of elastic waves for microseismic imaging: Geophysical Journal International, **200**, 390–401, doi: 10.1093/gji/ggu398.

Duan, Y., and P. Sava, 2015, Scalar imaging condition for elastic reverse time migration: Geophysics, **80**, no. 4, S127–S136, doi: 10.1190/geo2014-0453.1.

Duncan, P., and L. Eisner, 2010, Reservoir characterization using surface microseismic monitoring: Geophysics, **75**, no. 5, A139–A146, doi: 10.1190/1.3467760.

Eisner, L., D. Abbott, W. Barker, J. Lakings, and M. Thornton, 2008, Noise suppression for detection and location of microseismic events using a matched filter: 78th Annual International Meeting, SEG, Expanded Abstracts, 1431–1435, doi: 10.1190/1.3059184.

Fomel, S., P. Sava, I. Vlad, Y. Liu, and V. Bashkardin, 2013, Madagascar: open-source software project for multidimensional data analysis and reproducible computational experiments: Journal of Open Research Software, **1**, no. 1, e8, doi: 10.5334/jors.ag.

Gajewski, D., and E. Tessmer, 2005, Reverse modeling for seismic event characterization: Geophysical Journal International, **163**, 276–284, doi: 10.1111/j.1365-246X.2005.02732.x.

Golub, G. H., and C. F. V. Loan, 1996, Matrix computations, 3rd ed.: John Hopkins University Press.

Grechka, V., and W. Heigl, 2017, Microseismic monitoring: SEG.

Jeremic, A., J. Kurpan, M. Thornton, and P. Duncan, 2015, Passive seismic multicomponent imaging using geometrical optics theory: 85th Annual International Meeting, SEG, Expanded Abstracts, 2610–2614, doi: 10.1190/segam2015-5877756.1.

Jeremic, A., J. Kurpan, M. Thornton, and M. Mueller, 2014, Extending passive seismic imaging to account for source mechanism effects: 84th

Annual International Meeting, SEG, Expanded Abstracts, 3868–3871, doi: 10.1190/segam2014-0727.1.
Kao, H., and S. Shan, 2004, The source-scanning algorithm: Mapping the distribution of seismic sources in time and space: Geophysical Journal International, **157**, 589–594, doi: 10.1111/j.1365-246X.2004.02276.x.
Lanczos, C., 1970, The variational principles of mechanics, 4th ed.: Dover Publications.
Maxwell, S., 2010, Microseismic: Growth born from success: The Leading Edge, **29**, 338–343, doi: 10.1190/1.3353732.
Maxwell, S., 2014, Microseismic imaging of hydraulic fracturing: Improved engineering of unconventional shale reservoirs: SEG, doi: 10.1190/1.9781560803164.
Maxwell, S., J. Rutledge, R. Jones, and M. Fehler, 2010, Petroleum reservoir characterization using downhole microseismic monitoring: Geophysics, **75**, no. 5, A129–A137, doi: 10.1190/1.3477966.
McMechan, G. A., 1982, Determination of source parameters by wavefield extrapolation: Geophysical Journal International, **71**, 613–628, doi: 10.1111/j.1365-246X.1982.tb02788.x.
Michel, O. J., and I. Tsvankin, 2013, Gradient computation for full-waveform inversion of microseismic data in VTI media: 83rd Annual International Meeting, SEG, Expanded Abstracts, 2238–2242, doi: 10.1190/segam2013-0701.1.
Morse, P., and H. Feshbach, 1953, Methods of theoretical physics: McGraw-Hill 1.
Mulder, W., and A. ten Kroode, 2002, Automatic velocity analysis by differential semblance optimization: Geophysics, **67**, 1184–1191, doi: 10.1190/1.1500380.
Nakata, N., and G. C. Beroza, 2016, Reverse time migration for microseismic sources using the geometric mean as an imaging condition: Geophysics, **81**, no. 2, KS51–KS60, doi: 10.1190/geo2015-0278.1.
Ravasi, M., and A. Curtis, 2013, Elastic imaging with exact wavefield extrapolation for application to ocean-bottom 4C seismic data: Geophysics, **78**, no. 6, S265–S284, doi: 10.1190/geo2013-0152.1.
Rickett, J., and P. Sava, 2002, Offset and angle-domain common image-point gathers for shot-profile migration: Geophysics, **67**, 883–889, doi: 10.1190/1.1484531.
Rocha, D., N. Tanushev, and P. Sava, 2016a, Acoustic wavefield imaging using the energy norm: Geophysics, **81**, no. 4, S151–S163, doi: 10.1190/geo2015-0486.1.
Rocha, D., N. Tanushev, and P. Sava, 2016b, Isotropic elastic wavefield imaging using the energy norm: Geophysics, **81**, no. 4, S207–S219, doi: 10.1190/geo2015-0487.1.
Rocha, D., N. Tanushev, and P. Sava, 2017, Anisotropic elastic wavefield imaging using the energy norm: Geophysics, **82**, no. 3, S225–S234, doi: 10.1190/geo2016-0424.1.
Saenger, E. H., 2011, Time reverse characterization of sources in heterogeneous media: NDT and E International, **44**, 751–759, doi: 10.1016/j.ndteint.2011.07.011.
Sava, P., and S. Fomel, 2006, Time-shift imaging condition in seismic migration: Geophysics, **71**, no. 6, S209–S217, doi: 10.1190/1.2338824.
Sava, P., and I. Vasconcelos, 2011, Extended imaging condition for wave-equation migration: Geophysical Prospecting, **59**, 35–55, doi: 10.1111/j.1365-2478.2010.00888.x.
Slawinski, M. A., 2003, Seismic waves and rays in elastic media: Elsevier Science, 34.
Sripanich, Y., S. Fomel, J. Sun, and J. Cheng, 2015, Elastic wave-vector decomposition in orthorhombic media: 85th Annual International Meeting, SEG, Expanded Abstracts, 498–503, doi: 10.1190/segam2015-5878063.1.
Steiner, B., E. H. Saenger, and S. M. Schmalholz, 2008, Time reverse modeling of low-frequency microtremors: Application to hydrocarbon reservoir localization: Geophysical Research Letters, **35**, L03–L07, doi: 10.1029/2007GL032097.
Symes, W., and J. Carazzone, 1991, Velocity inversion by differential semblance optimization: Geophysics, **56**, 654–663, doi: 10.1190/1.1443082.
Wang, W., G. A. McMechan, C. Tang, and F. Xie, 2016, Up/down and P/S decompositions of elastic wavefields using complex seismic traces with applications to calculating Poynting vectors and angle-domain common-image gathers from reverse time migrations: Geophysics, **81**, no. 4, S181–S194, doi: 10.1190/geo2015-0456.1.
Warpinski, N. R., J. Du, and U. Zimmer, 2012, Measurements of hydraulic-fracture-induced seismicity in gas shales: SPE Production and Operations, **27**, 240–252, doi: 10.2118/151597-PA.
Weiss, R. M., and J. Shragge, 2013, Solving 3D anisotropic elastic wave equations on parallel GPU devices: Geophysics, **78**, no. 2, F7–F15, doi: 10.1190/geo2012-0063.1.
Witten, B., and B. Artman, 2010, Signal-to-noise estimates of time-reverse images: 80th Annual International Meeting, SEG, Expanded Abstracts, 2176–2180, doi: 10.1190/1.3513276.
Witten, B., and J. Shragge, 2015, Extended wave-equation imaging conditions for passive seismic data: Geophysics, **80**, no. 6, WC61–WC72, doi: 10.1190/geo2015-0046.1.
Witten, B., and J. Shragge, 2017a, Image-domain velocity inversion and event location for microseismic monitoring: Geophysics, **82**, no. 5, KS71–KS83, doi: 10.1190/geo2016-0561.1.
Witten, B., and J. Shragge, 2017b, Microseismic image-domain velocity inversion: Marcellus Shale case study: Geophysics, **82**, no. 6, KS99–KS112, doi: 10.1190/geo2017-0263.1.
Xuan, R., and P. Sava, 2010, Probabilistic microearthquake location for reservoir monitoring: Geophysics, **75**, no. 3, MA9–MA26, doi: 10.1190/1.3417757.
Yan, J., and P. Sava, 2008, Isotropic angle-domain elastic reverse-time migration: Geophysics, **73**, no. 6, S229–S239, doi: 10.1190/1.2981241.
Yan, J., and P. Sava, 2009, Elastic wave-mode separation for VTI media: Geophysics, **74**, no. 5, WB19–WB32, doi: 10.1190/1.3184014.
Yan, J., and P. Sava, 2011, Elastic wave-mode separation for tilted transverse isotropy media: Geophysical Prospecting, **60**, 29–48.
Yang, T., and P. Sava, 2011, Wave-equation migration velocity analysis with time-lag imaging: Geophysical Prospecting, **59**, 635–650.
Yang, T., and P. Sava, 2015, Image-domain wavefield tomography with extended common-image-point gathers: Geophysical Prospecting, **63**, 1086–1096, doi: 10.1111/1365-2478.12204.
Yang, T., J. Shragge, and P. Sava, 2013, Illumination compensation for image-domain wavefield tomography: Geophysics, **78**, no. 5, U65–U76, doi: 10.1190/geo2012-0278.1.
Yu, Y.-Y., 1964, Generalized Hamilton's principle and variational equation of motion in nonlinear elasticity theory, with application to plate theory: The Journal of the Acoustic Society of America, **36**, 111–120.
Zhang, Q., and G. A. McMechan, 2010, 2D and 3D elastic wavefield vector decomposition in the wavenumber domain for VTI media: Geophysics, **75**, no. 3, D13–D26, doi: 10.1190/1.3431045.
Zhebel, O., and L. Eisner, 2015, Simultaneous microseismic event localization and source mechanism determination: Geophysics, **80**, no. 1, KS1–KS9, doi: 10.1190/geo2014-0055.1.

Downloaded 03/14/19 to 138.67.129.23. Redistribution subject to SEG license or copyright; see Terms of Use at http://library.seg.org/